The Astrophysical Journal, 776:119 (7pp), 2013 October 20 doi:10.1088/0004-637X/776/2/119

A REVERSE SHOCK IN GRB 130427A

T. Laskar[1], E. Berger[1], B. A. Zauderer[1], R. Margutti[1], A. M. Soderberg[1], S. Chakraborti[1], R. Lunnan[1], R. Chornock[1], P. Chandra[2], and A. Ray[3]
[1] Harvard-Smithsonian Center for Astrophysics, 60 Garden Street, Cambridge, MA 02138, USA
[2] National Centre for Radio Astrophysics, Tata Institute of Fundamental Research, Pune University Campus, Ganeshkhind, Pune 411 007, India
[3] Tata Institute of Fundamental Research, Homi Bhabha Road, Mumbai 400 005, India
Received 2013 May 11; accepted 2013 August 10; published 2013 October 7

ABSTRACT

We present extensive radio and millimeter observations of the unusually bright GRB 130427A at $z = 0.340$, spanning 0.67–12 days after the burst. We combine these data with detailed multi-band UV, optical, NIR, and *Swift* X-ray observations and find that the broadband afterglow emission is composed of distinct reverse shock and forward shock contributions. The reverse shock emission dominates in the radio/millimeter and at $\lesssim$0.1 days in the UV/optical/NIR, while the forward shock emission dominates in the X-rays and at $\gtrsim$0.1 days in the UV/optical/NIR. We further find that the optical and X-ray data require a wind circumburst environment, pointing to a massive star progenitor. Using the combined forward and reverse shock emission, we find that the parameters of the burst include an isotropic kinetic energy of $E_{\rm K,iso} \approx 2 \times 10^{53}$ erg, a mass loss rate of $\dot{M} \approx 3 \times 10^{-8}\ M_\odot\ {\rm yr}^{-1}$ (for a wind velocity of 1000 km s^{-1}), and a Lorentz factor at the deceleration time of $\Gamma(200\,{\rm s}) \approx 130$. Due to the low density and large isotropic energy, the absence of a jet break to ≈15 days places only a weak constraint on the opening angle, $\theta_{\rm j} \gtrsim 2.^\circ5$, and therefore a total energy of $E_\gamma + E_K \gtrsim 1.2 \times 10^{51}$ erg, similar to other gamma-ray bursts (GRBs). The reverse shock emission is detectable in this burst due to the low circumburst density, which leads to a slow cooling shock. We speculate that this property is required for the detectability of reverse shocks in radio and millimeter bands. Following on GRB 130427A as a benchmark event, observations of future GRBs with the exquisite sensitivity of the Very Large Array and ALMA, coupled with detailed modeling of the reverse and forward shock contributions, will test this hypothesis.

Key word: gamma-ray burst: individual (GRB 130427A)

Online-only material: color figures

1. INTRODUCTION

Although long-duration gamma-ray bursts (GRBs) have been associated with the deaths of massive stars (Woosley & Bloom 2006), the precise nature of their progenitors, the structure of their explosion environments, and the composition of their ejecta remain only partially explored. Studies of the afterglow (forward shock, FS) emission provide insight into the explosion energy, geometry, and the structure of the circumburst medium (e.g., Sari et al. 1998; Chevalier & Li 2000). On the other hand, the most useful probe of the initial bulk Lorentz factor and the ejecta composition is afforded by the reverse shock (RS), which is expected to produce a similar synchrotron spectrum as the FS, with well-defined properties relative to the FS (e.g., Sari & Piran 1999b; Kobayashi & Zhang 2003a; Zou et al. 2005).

The expected observational signature of the RS is early time flares in the optical and radio bands and several studies have found hints of excess early-time emission attributable to a RS like component (e.g., Akerlof et al. 1999; Sari & Piran 1999a; Kulkarni et al. 1999; Soderberg & Ramirez-Ruiz 2002, 2003; Kobayashi & Zhang 2003b; Berger et al. 2003; Chevalier et al. 2004). However, a detailed understanding of RS emission requires a careful decomposition of the afterglow spectral energy distribution (SED) into RS and FS components. Since the peak frequencies of the two components are related by a factor of $\Gamma^2 \gtrsim 10^4$, such a decomposition requires multi-wavelength observations spanning several orders of magnitude in frequency. Similarly, the density profile of the environment affects the hydrodynamical evolution of both the FS and the RS, leading to discernible differences in the behavior of the light curves. Consequently, well-sampled light curves are also essential for any systematic study of RSs.

Such datasets have not been available to date primarily due to sensitivity limitations of radio and millimeter facilities. However, the recent upgrade of the Very Large Array to the Karl G. Jansky Very Large Array (VLA), with an order of magnitude improvement in sensitivity, has opened a new avenue for the study of RSs in GRBs. Here we present the first example of a RS detected in a multi-wavelength dataset spanning 1–100 GHz of the nearby energetic GRB 130427A. By combining our detailed radio and millimeter observations with X-ray data from *Swift* and UV/optical/near-infrared (NIR) observations from *Swift* and ground-based telescopes, we present the most comprehensive dataset for RS studies to date. We undertake a joint model fit to the entire dataset and extract parameters for the explosion and the environment and draw general conclusions on RS studies in the VLA and ALMA era.

2. OBSERVATIONS AND DATA ANALYSIS

2.1. GRB Discovery

GRB 130427A was discovered by the *Swift* (Gehrels et al. 2004) Burst Alert Telescope (BAT; Barthelmy et al. 2005) on 2013 April 27 at 07:17:57 UT (Maselli et al. 2013) with a duration of $T_{90} = 163$ s and a fluence of $F_\gamma = 3.1 \times 10^{-4}$ erg cm^{-2} (15–150 keV; Barthelmy et al. 2013). The burst was also detected with the *Fermi* Gamma-ray Burst Monitor (GBM; Meegan et al. 2009), 50.6 s before the *Swift* trigger[4] with an unusually large fluence of $F_\gamma = 2 \times 10^{-3}$ erg cm^{-2} (10–1000 keV) and a peak energy of $E_{\rm p} = 830$ keV (von Kienlin 2013). Coincident high-energy gamma-ray emission

[4] In our analysis, we take the GBM trigger time as the start time of the event, t_0.

was detected by the *Fermi* Large Area Telescope (Atwood et al. 2009) up to 94 GeV (Zhu et al. 2013).

The *Swift* X-Ray Telescope (XRT; Burrows et al. 2005) began observing the field 140 s after the BAT trigger, leading to the detection of the X-ray afterglow, localized to R.A.(J2000) = $11^{h}32^{m}32\overset{s}{.}63$, decl.(J2000) = $+27^{d}41^{m}51\overset{s}{.}7$, with an uncertainty radius of 3.5 arcsec (90% containment; Kennea et al. 2013). The *Swift* UV/Optical Telescope (UVOT; Roming et al. 2005) began observing the field 150 s after the burst, leading to the detection of a bright UV/optical afterglow (Maselli et al. 2013), which was subsequently detected by several ground-based observatories in the optical (e.g., Elenin et al. 2013; Perley 2013b; Melandri et al. 2013; Morgan 2013; Yatsu et al. 2013), NIR (Morgan 2013), millimeter (Zauderer et al. 2013b; Perley 2013a), and radio (Zauderer et al. 2013a; Volvach et al. 2013; Chandra 2013; Corsi 2013). Spectra were obtained at Gemini-North, the Nordic Optical Telescope, and the Very Large Telescope, resulting in a redshift of $z = 0.340$ (Levan et al. 2013; Xu et al. 2013; Flores et al. 2013) and leading to an isotropic equivalent gamma-ray energy of $(1.05 \pm 0.15) \times 10^{54}$ erg ($E_{\gamma,\rm iso} = 1$–10^{4} keV, rest frame; Amati et al. 2013; Kann & Schulze 2013).

2.2. Radio to X-Ray Observations

We observed the position of GRB 130427A beginning on 2013 April 27.99 UT ($\Delta t = 0.67$ days) with the VLA at a mean frequency of 5.8 GHz and with the Combined Array for Research in Millimeter Astronomy (CARMA; Bock et al. 2006) beginning on 2013 April 28.13 UT ($\Delta t = 0.81$ days) at a mean frequency of 85 GHz. In both observations, we detect a strong radio source coincident with the optical afterglow position. The data were obtained in the standard continuum modes utilizing the VLA's WIDAR correlator (Perley et al. 2011) with a total bandwidth of ∼2 GHz and CARMA's continuum mode with a bandwidth of ∼8 GHz. For the VLA observations, we utilized 3C 286 for bandpass and flux calibration and J1125+2610 for gain calibration in all but one epoch, where J1159+2914 was utilized as the gain calibrator for observing frequencies greater than 15 GHz. For all CARMA observations, we utilized 3C 273 for primary flux calibration and 0854+201 for bandpass calibration. For gain calibration, we utilized 1224+213 and a source-gain cycle of ∼15 minutes. We analyzed the VLA observations using the Common Astronomy Software Applications (McMullin et al. 2007) and the Astronomical Image Processing System (AIPS; Greisen 2003). We analyzed the CARMA observations using the Multi-channel Image Reconstruction, Image Analysis, and Display software (Sault et al. 1995). In all cases, we flagged edge channels and any data corrupted with radio frequency interference. We measured the flux density of the afterglow in the final images using the AIPS task JMFIT. We also observed GRB 130427A with the Giant Metrewave Radio Telescope (GMRT) at central frequencies of 1390 MHz and 610 MHz (bandwidth of 32 MHz), using J1125+261 and J1227+365 as phase calibrators and 3C 147 and 3C 286 as flux and bandpass calibrators, respectively. We analyzed the data using AIPS. A summary of all radio and millimeter observations is provided in Table 1.

We extracted *Swift*/XRT spectra at the times of our radio observations (at 58, 173, 406, and 786 ks) using the latest version of the HEASOFT package (ver. 6.13) and corresponding calibration files, following standard procedures (Evans et al. 2007, 2009; Margutti et al. 2013). The spectra are well fit by an absorbed single power-law model with $N_{\rm H,Gal} = 1.80 \times 10^{20}{\rm cm}^{-2}$ (Kalberla et al. 2005), an intrinsic hydrogen column $N_{\rm H,int} = (6.7 \pm 1.1) \times 10^{20}{\rm cm}^{-2}$, and a photon index $\Gamma = 1.76 \pm 0.03$ (68% confidence intervals). We find no statistically significant evidence for spectral evolution. We obtained XRT light curves by converting the 0.3–10 keV count rates reported on the *Swift* website[5] to a flux density at 1 keV using the measured spectral model (Evans et al. 2007, 2009).

Swift/UVOT observed GRB 130427A in six filters spanning the central wavelength range $\lambda_c = 1928$ Å ($w2$) to $\lambda_c = 5468$ Å(v). We analyzed the UVOT data using the latest version of HEASOFT, with corresponding calibration files and a 5″ aperture. The *Swift* star trackers failed to find a correct aspect solution during the first 1.9 ks of exposure. For these data, we manually checked each frame and corrected the position of the extraction region to account for the drifting of the source. The source point spread function appears to be highly distorted in the first two frames acquired in the v-band, while the first frames in the b- and u-bands suffer from significant coincidence losses

Table 1
Radio and Millimeter Observations of GRB 130427A

$t - t_0$ (days)	Observatory	Band	Frequency (Hz)	Flux Density (mJy)	Uncertainty (mJy)
0.67	VLA	C	5.1×10^{9}	1.5	0.075
0.67	VLA	C	6.8×10^{9}	2.5	0.125
2.00	VLA	C	5.1×10^{9}	1.82	0.091
2.00	VLA	C	6.8×10^{9}	1.76	0.088
2.00	VLA	K	1.92×10^{10}	1.31	0.0654
2.00	VLA	K	2.45×10^{10}	1.28	0.0639
2.00	VLA	Ku	1.35×10^{10}	1.48	0.0741
2.00	VLA	Ku	1.45×10^{10}	1.42	0.0708
4.70	VLA	C	5.1×10^{9}	0.621	0.0311
4.70	VLA	C	6.8×10^{9}	0.626	0.0313
4.70	VLA	Ku	1.35×10^{10}	0.552	0.0276
4.70	VLA	Ku	1.45×10^{10}	0.527	0.0264
4.70	VLA	K	1.92×10^{10}	0.469	0.0273
4.70	VLA	K	2.16×10^{10}	0.508	0.029
9.70	VLA	C	7.29×10^{9}	0.416	0.0352
9.70	VLA	X	8.4×10^{9}	0.357	0.0434
9.70	VLA	Ku	1.35×10^{10}	0.37	0.027
9.70	VLA	Ku	1.45×10^{10}	0.37	0.021
9.70	VLA	K	1.92×10^{10}	0.38	0.0475
9.70	VLA	K	2.45×10^{10}	0.43	0.0376
9.70	VLA	Ka	3.6×10^{10}	0.427	0.046
3.25	GMRT	L	1.39×10^{9}	0.50	0.10
4.83	GMRT	610	6.1×10^{8}	<0.30	...
5.40	GMRT	610	6.1×10^{8}	<0.26	...
11.6	GMRT	L	1.39×10^{9}	0.45	0.1
0.77	CARMA[a]	3 mm	9.25×10^{10}	3.7	0.4
0.81	CARMA	3 mm	8.5×10^{10}	3	0.3
1.00	CARMA[a]	3 mm	9.25×10^{10}	2.6	0.4
1.84	CARMA	3 mm	8.5×10^{10}	0.9	0.25
2.90	CARMA	3 mm	8.5×10^{10}	<0.72	...
4.81	MMT	g'	6.29×10^{14}	0.0313	0.00334
4.81	MMT	r'	4.56×10^{14}	0.0441	0.0047
4.82	MMT	i'	3.72×10^{14}	0.0433	0.00461
6.81	MMT	g'	6.29×10^{14}	0.0201	0.00215
6.81	MMT	r'	4.56×10^{14}	0.0308	0.00328
6.82	MMT	i'	3.72×10^{14}	0.0353	0.00377
11.0	MMT	g'	6.29×10^{14}	0.0163	0.00174
11.0	MMT	r'	4.56×10^{14}	0.0227	0.00242
11.0	MMT	i'	3.72×10^{14}	0.0215	0.00251

Notes. All limits are at 3σ.
[a] Perley (2013a).

[5] http://www.swift.ac.uk/xrt_curves/00554620/

due to the brightness of the afterglow. We do not use these exposures in our analysis.

We also obtained three epochs of $g'r'i'$ photometry of the optical afterglow using the MMTcam imager on the MMT 6.5 m telescope.[6] A sequence of 2×150 s dithered images in each band was taken on 2013 May 2.43 UT, 2×250 s (in g' and r') and 2×300 s (in i') on 2013 May 4.43 UT, and 3×300 s in each band on 2013 May 8.44 UT. The images were bias- and dark-subtracted, flat-fielded, and stacked using standard routines in IRAF.[7] The combined flux of the GRB and host galaxy was measured using aperture photometry with an aperture size of 2.5 times the seeing of the images and calibrated relative to the Sloan Digital Sky Survey (SDSS) photometry of the nearby star SDSS J113231.32+274222.7. We list these observations in Table 1.

Finally, we collected all publicly available photometry from the GRB Coordinates Network (GCN) Circulars and converted the reported magnitudes to flux densities at the following central wavelengths: g' : 445 nm, V : 551 nm, R : 658 nm, I : 806 nm, z' : 900 nm, Y : 1020 nm, J : 1220 nm, H : 1630 nm, and K : 2190 nm. For magnitudes reported in the Vega system, we used the zeropoints from Bessell et al. (1998).

3. BASIC CONSIDERATIONS

We interpret the observed behavior of the afterglow emission from radio to X-rays in the framework of the standard synchrotron model, described by three break frequencies (the self-absorption frequency: ν_a, the characteristic synchrotron frequency: ν_m, and the synchrotron cooling frequency: ν_c) and an overall flux normalization. In this model, there are well-defined relations between the temporal evolution and spectral indices that allow us to determine the location of the synchrotron frequencies as well as the density profile of the circumburst medium (interstellar medium (ISM) profile: $\rho=$ const; wind: $\rho\propto r^{-2}$). The models are described in detail in Sari et al. (1998) and Chevalier & Li (2000).

A striking feature of the afterglow light curves is the unbroken power-law decline in the X-rays with $\alpha_X\approx-1.35$ at $\gtrsim$200 s ($F_\nu\propto t^\alpha$). Given the X-ray spectral index of $\beta_X\approx-0.76$ during this time ($F_\nu\propto\nu^\beta$), we expect an X-ray decline rate of $\alpha_X=-0.64$ if $\nu_c<\nu_X$ (independent of the circumburst density profile), while for $\nu_c>\nu_X$, we expect $\alpha_X\approx-1.14$ for an ISM profile or $\alpha_X\approx-1.64$ for a wind profile. Since the decline rate predicted in the ISM model is shallower than the observed value independent of the ordering of ν_c and ν_X, we conclude that a wind profile is required, with $\nu_c\sim\nu_X$ providing a reasonable match to the observed decline. This conclusion is further supported by the similar decline rate in the UV/optical/NIR bands at $\gtrsim$0.3 days, $\alpha_{opt}\approx-1.35$, which indicates that the optical and X-ray bands are located on the same portion of the synchrotron spectrum (i.e., $\nu_m<\nu_{opt}<\nu_X\sim\nu_c$). Indeed, as shown with the broadband SEDs in Figure 1, the NIR/X-ray spectral index at ≈2.0 days is $\beta_{NIR,X}\approx-0.70$, in agreement with our conclusion that the optical and X-ray bands are located on the same synchrotron slope. On the other hand, the spectral index within the UV/optical/NIR bands, $\beta_{opt}\approx-0.85$, is steeper, indicating that modest extinction is present. The observed optical and X-ray decline rates require an electron power-law index of $p\approx2.2$, consistent with the observed X-ray spectral index given the proximity of the cooling break. We note that in the wind model $\nu_c\propto t^{1/2}$ and hence once ν_c crosses the X-ray band, the X-ray flux is expected to decline as an unbroken power law, matching the observed behavior.

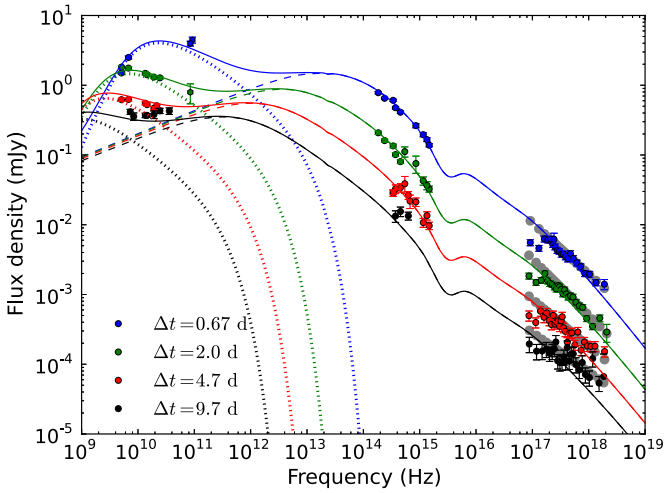

Figure 1. Spectral energy distribution of the afterglow at $\Delta t=0.67$, 2.0, 4.7, and 9.7 days. The optical data are small extrapolations from the nearest available data points with a power law of $t^{-1.35}$. The dip in the model around 3×10^{15} Hz is caused by extinction ($A_V=0.18$ mag) in the host galaxy. The light gray points represent the unabsorbed models for the X-ray spectra. The dashed and dotted curves show the spectrum of the forward shock and reverse shocks, respectively, while the solid lines are the sum of the two. The combined model fully captures the observed evolution across nine orders of magnitude in frequency.

(A color version of this figure is available in the online journal.)

Finally, a 24.5 GHz radio observation at $\Delta t\approx29$ days with a flux density of 0.16 ± 0.03 mJy also strongly rules out the ISM environment, since $\nu_m<\nu_{NIR}$ at 0.3 days and the NIR K-band flux density is ≈1.6 mJy at this time, which together predict a flux density $\gtrsim$0.9 mJy at 24.5 GHz at ≈29 days in the ISM model. We defer a complete analysis of the observations after ≈15 days to a future work.

Whereas the X-ray light curve follows a single power-law decline, the UV/optical/NIR light curves display a clear change in slope at ≈0.1 days (see Figure 2). The initial slope is shallower, with $\alpha_{opt}\approx-0.8$, and the time of the break is chromatic, occurring later in the redder filters. In the wind model, the passage of ν_m through an observing band results in a transition from $\alpha=0$ to $\alpha=(1\text{–}3p)/4\approx-1.4$ (for $p=2.2$), in clear contrast with the observed evolution. This result indicates that a different emission component dominates the UV/optical/NIR light curves at $\lesssim$0.1 days.

Even stronger evidence for a distinct emission component is provided by the radio and millimeter data. The relatively flat spectral index between the radio/millimeter and optical bands at all times, $\beta_{radio,opt}\approx-0.25$, is inconsistent with a single power-law extrapolation from the optical. This shallow slope cannot be caused by the location of ν_m between the radio and optical bands because all light curves below ν_m should be flat in the wind model, while the observed radio and millimeter light curves clearly decline at all frequencies spanning 6.8–90 GHz. Similarly, the expected spectral index below ν_m is $\beta=1/3$ or 2 (the latter if ν_a is located above an observing band), while we observe instead $\beta_{radio}\approx-0.2$ at $\Delta t\approx2$–5 days (Figure 1).

One way to flatten the spectral slope between the radio and optical bands is to introduce a break in the electron energy

[6] http://www.cfa.harvard.edu/mmti/wfs.html

[7] IRAF is distributed by the National Optical Astronomy Observatory, which are operated by the Association of Universities for Research in Astronomy, Inc., under cooperative agreement with the National Science Foundation.

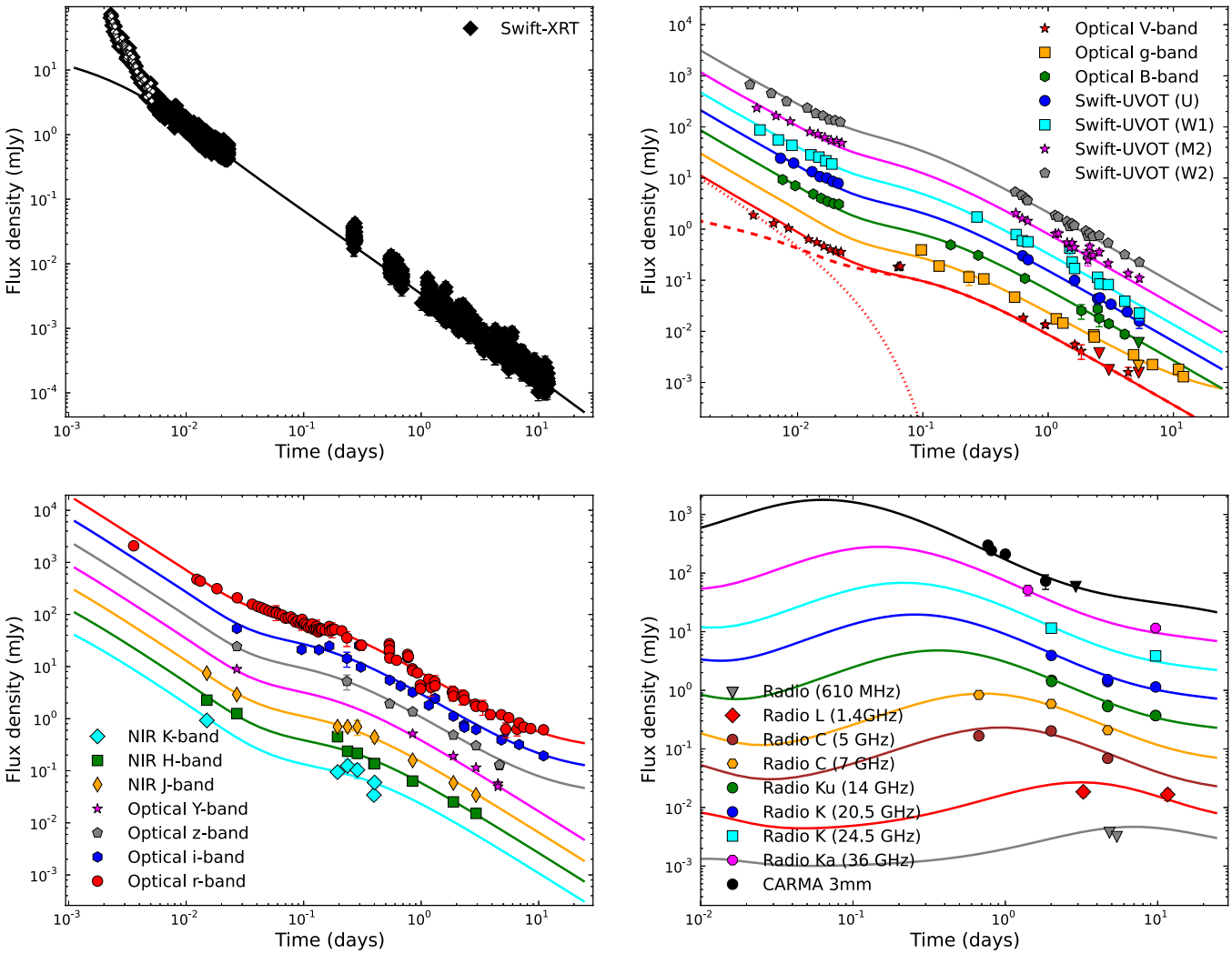

Figure 2. Light curves of the afterglow along with the combined RS plus FS model (lines). Top left: *Swift*/XRT; top right: *Swift*/UVOT and ground-based *g*-band; bottom left: ground-based *rizYJHK* observations from MMTcam and as reported in GCN Circulars; bottom right: GMRT, VLA, and CARMA observations spanning 0.6–90 GHz. Adjacent light curves have been offset by a factor of three for visual clarity (*U*, *Y*, and the radio *Ku* band remain on the correct scale). In the top right panel, we show a decomposition of the *V*-band light curve into RS (dotted) and FS (dashed) components to guide the reader. The *Swift*/XRT data show a steep-to-shallow transition around $\Delta t = 450$ s, which cannot be explained in our model. These data (open symbols) are likely dominated by the low-energy tail of the prompt emission and we exclude them from our fit.

(A color version of this figure is available in the online journal.)

distribution at γ_b such that $N(\gamma) \propto \gamma^{-p_2}$ (with $p_2 < 2$) for $\gamma_m < \gamma < \gamma_b$ and such that $\nu_{syn}(\gamma_m) \lesssim 1$ GHz at $\Delta t \lesssim 9.7$ days, where $\nu_{syn}(\gamma)$ is the characteristic synchrotron frequency corresponding to electrons with a Lorentz factor γ. For the observed value of $\beta_{radio,opt}$, $p_2 \approx 1.4$ is required. However, in this scenario, the radio spectral index can only remain constant (before the passage of $\nu_{syn}(\gamma_b)$ through the radio band) or steepen with time (after the passage of $\nu_{syn}(\gamma_b)$). Instead, we observe that the radio spectral index becomes shallower from $\beta_{radio} = -0.25 \pm 0.02$ at 2.0 days to $\beta_{radio} = -0.09 \pm 0.07$ at 9.7 days. This fact argues against a break in the electron spectrum causing the shallow radio/optical spectral slope.

Instead, the distinct spectral and temporal behavior in the radio and millimeter clearly requires a different emission component, which is also required to explain the UV/optical/NIR data at $\lesssim$0.1 days. We associate this component with the RS and show in detail in the next section that it can explain the radio and millimeter data as well as the early optical data. To gain insight into the RS spectrum, we note that the SED at 0.67 days (Figure 1) requires ν_m to be located between 10 and 90 GHz, with an optically thin spectrum extending to the optical. In addition, the spectral index between 5.1 and 6.8 GHz, $\beta \approx 1.8$, is indicative of self-absorption, with $\nu_a \approx 7$ GHz. The optically thin spectrum observed in the radio at about 2.0 days indicates that $\nu_a \lesssim 5$ GHz at that time. Additionally, since the emission from a RS cuts off exponentially above ν_c, whereas we invoke some contribution from this component to the UV flux at $\lesssim$0.1 days, we require $\nu_c \gtrsim 10^{15}$ Hz for the RS at $\approx$0.1 days.

To summarize, the optical data at $\gtrsim$0.1 days, when combined with the full X-ray light curve at $\gtrsim$200 s, require a wind medium with $p \approx 2.2$, $\nu_c \sim \nu_X$, and $\nu_m \sim \nu_{opt}$ at ~ 0.1 days. In addition, the radio and millimeter emission and the early optical emission at $\lesssim$0.1 days cannot be accommodated by same synchrotron spectrum and therefore require a separate emission component. This emission component has $\nu_a \approx 7$ GHz and $\nu_m \approx$ 10–90 GHz at 0.67 days, as well as $\nu_c \approx 10^{15}$ Hz at 0.1 days. In the next section, we expand on these results with full broadband modeling of the FS and RS emission.

4. A SELF-CONSISTENT REVERSE SHOCK/FORWARD SHOCK MODEL

Based on the basic considerations described in the previous section, we construct a model SED for the radio to X-ray emission at 0.67 days (Figure 1). The model is composed of two emission components: (1) a FS, which peaks between the millimeter and optical bands, fits the NIR to X-ray SED, and provides negligible contribution in the radio/millimeter and (2) a RS, which fits the radio to millimeter SED and provides negligible contribution at higher frequencies. The synchrotron parameters of the RS are $\nu_{\rm a,RS} \approx 7$ GHz, $\nu_{\rm m,RS} \approx 20$ GHz, $\nu_{\rm c,RS} \approx 10^{13}$ Hz, and $F_{\nu \rm m,RS} \approx 10$ mJy. The synchrotron parameters describing the FS are $\nu_{\rm a,FS} < 5$ GHz, $\nu_{\rm m,FS} \approx 4 \times 10^{13}$ Hz, $\nu_{\rm c,FS} \approx 2 \times 10^{17}$ Hz, and $F_{\nu,\rm m,FS} \approx 3$ mJy. Both SEDs are in the slow cooling regime with the standard ordering of the synchrotron break frequencies, $\nu_{\rm a} < \nu_{\rm m} < \nu_{\rm c}$. We find that this combined RS plus FS model with a common value of $p \approx 2.2$ completely describes the observed SED at 0.67 days (Figure 1).

We evolve both emission components in time to the other three epochs where we have extracted multi-wavelength SEDs. The evolution of the RS spectrum depends upon whether the shock is relativistic or Newtonian in the frame of the unshocked ejecta. Zou et al. (2005) derive the temporal evolution of the RS break frequencies, both before and after the ejecta crossing time (the so-called deceleration time, $t_{\rm dec}$) in the two asymptotic regimes of relativistic and Newtonian evolution. An important constraint on the shock evolution is provided by an R-band flux density of about 77 mJy measured by the Faulkes Telescope North at ≈4.3 minutes (Melandri et al. 2013). We find that a relativistic RS overpredicts this early optical emission by about a factor of five. In addition, in the relativistic case, both $\nu_{\rm m,RS}$ and $\nu_{\rm c,RS}$[8] evolve as $t^{-15/8}$, leading to a predicted decline rate of $t^{-3(5p+1)/16} \sim t^{-2.25}$ above $\nu_{\rm m,RS}$ (for $p = 2.2$), which is significantly steeper than the observed decline rate in the millimeter and radio bands, $\alpha_{\rm mm} \approx -1.5$ and $\alpha_{\rm radio} \approx -1.0$. Similarly, the decline rate below $\nu_{\rm m,RS}$ is predicted to be $t^{-1/2}$ in the relativistic RS model, which is much shallower than the observed decline rates. The Newtonian RS model, on the other hand, offers an additional degree of freedom via the profile of the shocked ejecta, $\gamma \propto r^{-g}$, where we expect $1/2 < g < 3/2$ from theoretical considerations (Zou et al. 2005). We treat g as a free parameter and find a good match to the SED evolution with $g \approx 5$. In the following, we focus on the Newtonian RS case.

Our implementation of the FS follows the smoothly connected power-law synchrotron spectrum for the wind environment of Granot & Sari (2002), where we compute the break frequencies and normalizations using the standard microphysical parameters (ϵ_e and ϵ_B), the explosion energy ($E_{\rm K,iso}$), and the circumburst density in the wind profile (A_*). We also use the Small Magellanic Cloud extinction curve (Pei 1992) to model the extinction in the host galaxy ($A_{\rm V}$). We use the flux density of the host galaxy in the *griz* filters as measured in the SDSS as an additive component to the relevant filters. Having determined a set of values for the break frequencies of the RS spectrum at 0.67 days, we evolve these parameters based on Newtonian evolution and fit separately for the FS contribution to the total flux at all frequencies. We determine the FS parameters by fitting all of the available photometry simultaneously with a combination of RS and FS spectra. To efficiently and rapidly sample the available parameter space, we carry out a Markov Chain Monte Carlo (MCMC) analysis using a Python implementation of the ensemble MCMC sampler EMCEE (Foreman-Mackey et al. 2013). For a detailed discussion of our modeling scheme, see Laskar et al. (2013).

[8] Here, $\nu_{\rm c}$ refers to $\nu_{\rm cut}$, the cutoff frequency above which RS emission is negligible owing to synchrotron cooling.

Table 2
Forward Shock Parameters for the Best Fit Wind Model

Parameter	Value
p	2.23
ϵ_e	$0.30(\nu_{\rm a}/14\,{\rm MHz})^{5/6}$
ϵ_b	$0.20(\nu_{\rm a}/14\,{\rm MHz})^{-5/2}$
A_*	$3.0 \times 10^{-3}(\nu_{\rm a}/14\,{\rm MHz})^{5/3}$
$E_{\rm K,iso,52}$	$4.9(\nu_{\rm a}/14\,{\rm MHz})^{-5/6}$
A_V	0.18 mag
Γ	130
$t_{\rm jet}$	$\gtrsim$15 days
$\theta_{\rm jet}$	$>2.^{\circ}5$
$\nu_{\rm a,FS}$	(12–16)×10^6 Hz
$\nu_{\rm m,FS}$	2.2×10^{13} Hz
$\nu_{\rm c,FS}$	2.8×10^{17} Hz
$\nu_{\rm a,RS}$	5.7×10^{9} GHz
$\nu_{\rm m,RS}$	1.2×10^{10} Hz
$\nu_{\rm c,RS}$	5.9×10^{12} Hz

Notes. All frequencies in this table are calculated at $\Delta t = 1$ day. The self-absorption frequency of the forward shock at 1 day, $\nu_{\rm a}$, is constrained to 12 MHz $< \nu_{\rm a} <$ 16 MHz by the requirement $\epsilon_{\rm e}, \epsilon_{\rm b} < 1/3$.

We find that the self-absorption frequency of the FS ($\nu_{\rm a,FS}$) declines below about 300 MHz 0.5 hr after the burst and is not directly observed thereafter. Consequently, the derived blastwave parameters are degenerate with respect to $\nu_{\rm a,FS}$; we quote all results in terms of this frequency, scaled to 14 MHz at 1 day (Table 2). Imposing the theoretical restrictions $\epsilon_e, \epsilon_B < 1/3$, we further constrain the blastwave parameters to the following narrow ranges: 12 MHz $< \nu_{\rm a,FS} <$ 16 MHz, $0.25 < \epsilon_e < 0.33$, $0.14 < \epsilon_B < 0.33$, $2.1 \times 10^{-3} < A_* < 3.7 \times 10^{-3}$, and $4.4 < E_{\rm K,iso,52} < 5.8$. Marginalizing the posterior density functions, we find the following median values of the FS parameters: $p = 2.23$, $\epsilon_{\rm e} = 0.30$, $\epsilon_B = 0.20$, $A_* = 2.9 \times 10^{-3}$, $E_{\rm K,iso,52} = 4.9$, and $A_{\rm V} = 0.18$ mag. The FS spectrum transitions from fast cooling to slow cooling around $\Delta t \approx 1200$ s. The best-fit combined RS and FS model is shown for the multi-epoch SEDs in Figure 1 and for all available radio to X-ray light curves in Figure 2. The model fully captures the observed evolution across nine orders of magnitude in frequency and over three orders of magnitude in time.

The bulk Lorentz factor of the ejecta, Γ, can be calculated from a knowledge of the deceleration time and the parameters of the explosion. In the internal–external shock model, we expect the deceleration time to roughly match the duration of the burst. Since the *Swift*/BAT $T_{90} \approx 163$ s and the optical flux is already declining at ≈258 s (Melandri et al. 2013), we take $t_{\rm dec} \approx 200$ s. Using the relation $t_{\rm dec} \approx 29(1+z)E_{\rm K,iso,52}\Gamma_{1.5}^{-4}A_*^{-1}$ s (Zou et al. 2005), we find $\Gamma \approx 120$–150 at $t_{\rm dec}$, where the range corresponds to the uncertainty in $E_{\rm K,iso,52}$ and A_* due to the uncertainty in $\nu_{\rm a,FS}$. For the median values of $E_{\rm K,iso,52}$ and A_* reported above, we obtain $\Gamma \approx 130$.

In the preceding analysis, we independently determined the RS break frequencies and fit for the parameters of the FS. However, the two synchrotron spectra are related since the

two shocks propagate in opposite directions from the contact discontinuity. In particular, we expect that at the deceleration time $\nu_{c,RS} \sim \nu_{c,FS}$, $\nu_{m,RS} \sim \nu_{m,FS}/\Gamma^2$ and $F_{\nu,m,RS} \sim \Gamma F_{\nu,m,FS}$. For the parameters given above, we find that the FS parameters at the deceleration time are $\nu_{c,FS} \approx 7.8 \times 10^{15}(t_{dec}/200\,s)^{1/2}$ Hz,[9] $\nu_{m,FS} \approx 2.2 \times 10^{17}(t_{dec}/200\,s)^{-3/2}$ Hz, and $F_{\nu,m,FS} \approx 13(t_{dec}/200\,s)^{1/2}$ mJy. For the RS, we have $\nu_{c,RS} \approx 1.5 \times 10^{16}(t_{dec}/200\,s)^{-1.3}$ Hz, $\Gamma^2\nu_{m,RS} \approx 5.3 \times 10^{17}(t_{dec}/200\,s)^{-1.3}(\Gamma/130)^2$ Hz, and $F_{\nu,m,RS}/\Gamma \approx 13(t_{dec}/200\,s)^{-0.9}(\Gamma/130)^{-1}$ mJy at the deceleration time, where the power-law indices for $\nu_{c,RS}$, $\nu_{m,RS}$, and $F_{\nu,m,RS}$ are derived from the g-dependent expressions in Zou et al. (2005). We thus confirm that the expected relations between the RS and FS parameters are satisfied to within a factor of two, confirming our basic assumption that the two required emission components indeed correspond to the RS and FS. Whereas our results are consistent with the shock microphysical parameters being the same in the FS and RS regimes, we note that these observations can accommodate magnetization parameters (Zhang et al. 2003; Harrison & Kobayashi 2013) in the range $1 \leqslant \sqrt{\epsilon_{B,RS}/\epsilon_{B,FS}} \lesssim 5$ for our fiducial values of Γ and t_{dec}. These limits are unfortunately degenerate with Γ and t_{dec} and we are unable to constrain these more strongly at this time.

To summarize, a model that includes emission from the RS and FS consistently explains all the available data from the radio to X-rays over a timescale of ∼200 s to ∼10 days. The resulting bulk Lorentz factor of the outflow at the deceleration time is $\Gamma \approx 130$.

5. CONCLUSIONS

We present a detailed multi-wavelength study of the bright afterglow of GRB 130427A spanning radio to X-rays. From the optical and X-ray data, we conclude that the progenitor exploded into a wind environment, pointing to a massive star. The radio and millimeter observations present a spectrum and temporal evolution that cannot be explained by emission from the FS alone. We show that this emission is consistent with synchrotron radiation from a Newtonian RS. With the available multi-band data, GRB 130427A is by far the best example to date of RS emission in the radio/millimeter, particularly when compared with previous detections that were based only on only one to two epochs at single frequencies (Kulkarni et al. 1999; Berger et al. 2003; Soderberg & Ramirez-Ruiz 2003). Our derived value of the index ($g \approx 5$) of the Lorentz factor profile of the shocked ejecta formally lies outside the expected range. The exquisite dataset available for this GRB provides a unique opportunity for a detailed study of RSs in wind environments, requiring the combined power of numerical simulations and multi-wavelength afterglow modeling. While beyond the scope of this work, such a study might potentially reconcile the large value of g with theoretical expectations, as well as shed light on the question of ejecta magnetization.

Using multi-wavelength model fitting of the rich afterglow dataset, with the well-sampled light curves spanning over three orders of magnitude in time and nine orders of magnitude in frequency, we determine the properties of the explosion and the circumburst medium. In particular, we find a low circumburst density, $A_* \approx 3 \times 10^{-3}$, corresponding to a mass loss rate of $\dot{M} = 3 \times 10^{-8}\,M_\odot\,\mathrm{yr}^{-1}$ (for a wind velocity of 1000 km s^{-1}). The low density causes the RS to be in the slow cooling regime ($\nu_{m,RS} < \nu_{c,RS}$), resulting in long-lived radio and millimeter emission. We note that a low density was also inferred for previous GRBs with likely radio RS emission (990123, 020405, and 021211; Chevalier et al. 2004), suggesting that low density is a requisite criterion for observable emission from a RS; in a high-density environment, the RS emission will decline rapidly due to efficient cooling of the radiating electrons (Kobayashi & Zhang 2003a).

From the derived properties of the explosion and environment, we obtain the Lorentz factor of the outflow at the deceleration time, $\Gamma(200\,s) \approx 130$, and show that the spectra of the FS and RS at the deceleration time are consistent with theoretical expectations. We infer $E_{K,iso} \approx 7 \times 10^{52}$ erg. However, we note that the FS spectrum transitions from fast to slow cooling at ≈1200 s and radiative corrections between this time and $t_{dec} \approx 200$ s are a factor of a few (Sari 1997; Dai & Lu 1998). This fact suggests that $E_{K,iso} \approx 2 \times 10^{53}$ erg, which is ≈20% of the isotropic-equivalent gamma-ray energy, implying a large radiative efficiency. The lack of an obvious break in the X-ray light curves to ≈15 days implies a lower limit of only $\theta_{jet} \gtrsim 2.^\circ5$ on the opening angle of the jet, and hence $E_K \gtrsim 2 \times 10^{50}$ erg and $E_{\gamma,} \gtrsim 10^{51}$ erg. Thus, due primarily to the combination of a large isotropic energy and a low circumburst density, the lack of a jet break at ≲15 days is not surprising.

We conclude by noting that GRB 130427A is likely to become the benchmark for RS studies in the VLA and ALMA era. Our study demonstrates that a complete analysis of the explosion and ejecta properties requires detailed multi-wavelength modeling to leverage the anticipated exquisite datasets.

We thank Shiho Kobayashi, Yuanchuan Zou, Xuefeng Wu, Zigao Dai, Richard Harrison, and the anonymous referee for their helpful comments on the manuscript. The Berger GRB group is supported by the National Science Foundation under Grant AST-1107973. The MMT Observatory is a joint facility of the Smithsonian Institution and the University of Arizona. The National Radio Astronomy Observatory is a facility of the National Science Foundation operated under cooperative agreement by Associated Universities, Inc. This work made use of data supplied by the UK Swift Science Data Centre at the University of Leicester. CARMA observations were taken as part of the CARMA Key Project, c0999, "A Millimeter View of the Transient Universe" (PI: B. A. Zauderer) and VLA observations were taken as part of programs 13A-046 (PI: E. Berger), 13A-411 (PI: A. Corsi), SE0851 (PI: A. Fruchter), and S50386 (PI: S. B. Cenko). Support for CARMA construction was derived from the states of California, Illinois, and Maryland, the James S. McDonnell Foundation, the Gordon and Betty Moore Foundation, the Kenneth T. and Eileen L. Norris Foundation, the University of Chicago, the Associates of the California Institute of Technology, and the National Science Foundation. Ongoing CARMA development and operations are supported by the National Science Foundation under a cooperative agreement, and by the CARMA partner universities. The GMRT is run by the National Centre for Radio Astrophysics of the Tata Institute of Fundamental Research.

[9] The mean of ν_3 and ν_{11}, defined in Granot & Sari (2002).

REFERENCES

Akerlof, C., Balsano, R., Barthelmy, S., et al. 1999, Natur, 398, 400
Amati, L., Dichiara, S., Frontera, F., & Guidorzi, C. 2013, GCN, 14503, 1
Atwood, W. B., Abdo, A. A., Ackermann, M., et al. 2009, ApJ, 697, 1071
Barthelmy, S. D., Barbier, L. M., Cummings, J. R., et al. 2005, SSRv, 120, 143

Barthelmy, S. D., Baumgartner, W. H., Cummings, J. R., et al. 2013, GCN, 14470, 1
Berger, E., Soderberg, A. M., Frail, D. A., & Kulkarni, S. R. 2003, ApJL, 587, L5
Bessell, M. S., Castelli, F., & Plez, B. 1998, A&A, 333, 231
Bock, D. C.-J., Bolatto, A. D., Hawkins, D. W., et al. 2006, Proc. SPIE, 6267, 626713
Breeveld, A. A., Landsman, W., Holland, S. T., et al. 2011, in AIP Conf. Proc. 1358, Gamma Ray Bursts 2010, ed. J. E. McEnery, J. L. Racusin, & N. Gehrels (Melville, NY: AIP), 373
Burrows, D. N., Hill, J. E., Nousek, J. A., et al. 2005, SSRv, 120, 165
Chandra, P. 2013, GCN, 14519, 1
Chevalier, R. A., & Li, Z.-Y. 2000, ApJ, 536, 195
Chevalier, R. A., Li, Z.-Y., & Fransson, C. 2004, ApJ, 606, 369
Corsi, A. 2013, GCN, 14522, 1
Dai, Z. G., & Lu, T. 1998, MNRAS, 298, 87
Elenin, L., Volnova, A., Savanevych, V., et al. 2013, GCN, 14450, 1
Evans, P. A., Beardmore, A. P., Page, K. L., et al. 2007, A&A, 469, 379
Evans, P. A., Beardmore, A. P., Page, K. L., et al. 2009, MNRAS, 397, 1177
Flores, H., Covino, S., Xu, D., et al. 2013, GCN, 14491, 1
Foreman-Mackey, D., Hogg, D. W., Lang, D., & Goodman, J. 2013, PASP, 125, 306
Gehrels, N., Chincarini, G., Giommi, P., et al. 2004, ApJ, 611, 1005
Granot, J., & Sari, R. 2002, ApJ, 568, 820
Greisen, E. W. 2003, in Information Handling in Astronomy—Historical Vistas, ed. A. Heck (Astrophysics and Space Science Library, Vol. 285; Dordrecht: Kluwer), 109
Harrison, R., & Kobayashi, S. 2013, ApJ, 772, 101
Kalberla, P. M. W., Burton, W. B., Hartmann, D., et al. 2005, A&A, 440, 775
Kann, D. A., & Schulze, S. 2013, GCN, 14580, 1
Kennea, J. A., Stroh, M. C., Burrows, D. N., et al. 2013, GCN, 14485, 1
Kobayashi, S., & Zhang, B. 2003a, ApJ, 597, 455
Kobayashi, S., & Zhang, B. 2003b, ApJL, 582, L75
Kulkarni, S. R., Frail, D. A., Sari, R., et al. 1999, ApJL, 522, L97
Laskar, T., Berger, E., Tanvir, N., et al. 2013, arXiv:1307.6586
Levan, A. J., Cenko, S. B., Perley, D. A., & Tanvir, N. R. 2013, GCN, 14455, 1
Margutti, R., Zaninoni, E., Bernardini, M. G., et al. 2013, MNRAS, 428, 729
Maselli, A., Beardmore, A. P., Lien, A. Y., et al. 2013, GCN, 14448, 1
McMullin, J. P., Waters, B., Schiebel, D., Young, W., & Golap, K. 2007, in ASP Conf. Ser. 376, Astronomical Data Analysis Software and Systems XVI, ed. R. A. Shaw, F. Hill, & D. J. Bell (San Francisco, CA: ASP), 127
Meegan, C., Lichti, G., Bhat, P. N., et al. 2009, ApJ, 702, 791
Melandri, A., Guidorzi, C., Gomboc, A., Japelj, J., & Mundell, C. G. 2013, GCN, 14452, 1
Morgan, A. N. 2013, GCN, 14453, 1
Pei, Y. C. 1992, ApJ, 395, 130
Perley, D. A. 2013a, GCN, 14494, 1
Perley, D. A. 2013b, GCN, 14451, 1
Perley, R. A., Chandler, C. J., Butler, B. J., & Wrobel, J. M. 2011, ApJL, 739, L1
Roming, P. W. A., Kennedy, T. E., Mason, K. O., et al. 2005, SSRv, 120, 95
Sari, R. 1997, ApJL, 489, L37
Sari, R., & Piran, T. 1999a, ApJL, 517, L109
Sari, R., & Piran, T. 1999b, ApJ, 520, 641
Sari, R., Piran, T., & Narayan, R. 1998, ApJL, 497, L17
Sault, R. J., Teuben, P. J., & Wright, M. C. H. 1995, in ASP Conf. Ser. 77, Astronomical Data Analysis Software and Systems IV, ed. Rs. A. Shaw, H. E. Payne, & J. J. E. Hayes (San Francisco, CA: ASP), 433
Soderberg, A. M., & Ramirez-Ruiz, E. 2002, MNRAS, 330, L24
Soderberg, A. M., & Ramirez-Ruiz, E. 2003, MNRAS, 345, 854
Volvach, A., Volvach, L., & Pozanenko, A. 2013, GCN, 14505, 1
von Kienlin, A. 2013, GCN, 14473, 1
Woosley, S. E., & Bloom, J. S. 2006, ARA&A, 44, 507
Xu, D., de Ugarte Postigo, A., Schulze, S., et al. 2013, GCN, 14478, 1
Yatsu, Y., Yano, Y., Usui, R., et al. 2013, GCN, 14454, 1
Zauderer, B. A., Berger, E., Chakraborti, S., & Soderberg, A. 2013a, GCN, 14480, 1
Zauderer, B. A., Berger, E., Chakraborti, S., & Soderberg, A. M. 2013b, GCN, 14482, 1
Zhang, B., Kobayashi, S., & Mészáros, P. 2003, ApJ, 595, 950
Zhu, S., Racusin, J., Kocevski, D., et al. 2013, GCN, 14471, 1
Zou, Y. C., Wu, X. F., & Dai, Z. G. 2005, MNRAS, 363, 93